Semi Annual Progress Report on

BLADE END WALL FLOWS IN COMPRESSORS

(NASA Grant NSG 3032)
(NASA - University Graduate Research Program in Aeronautics)

N. Sitaram and B. Lakshminarayana

To

National Aeronautics and Space Administration
Lewis Research Center
Project Monitor: P. M. Sockol

Department of Aerospace Engineering
The Pennsylvania State University
University Park, PA 16802

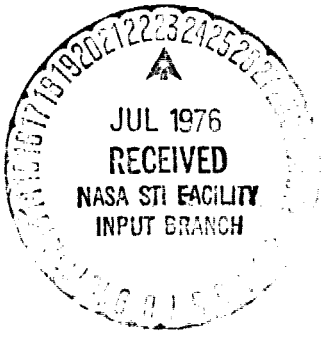

PREFACE

The research progress on the NASA Grant NSG 3032 is briefly reported here. The period covered is approximately nine months ending June 30, 1976. The research was initiated in September 1975.

The report is divided into four sections as follows.

1. Literature survey on the end wall flows in the axial flow compressors.
2. Analysis of the rotor blade end wall flows in the compressors.
3. Experimental facility, instrumentation and technique.
4. Status of the experimental work.

I. LITERATURE SURVEY ON ENDWALL FLOWS IN AXIAL FLOW COMPRESSORS

The flow near the tip region of a compressor rotor consists of secondary flows, casing boundary layer, blade boundary layer (including the radial migration of low momentum and energy flow), leakage flow and scraping vortex and hence is extremely complicated. The qualitative nature of end wall flows in a compressor rotor is illustrated in Fig. 1.

A brief summary of the previous work carried out on end wall flow phenomena will be presented in this section with major emphasis on annulus wall boundary layer.

A first serious attempt to incorporate boundary layer equations into compressor performance was made by Jansen (1), who simply applied the one-dimensional von-Karman momentum integral equation. Although some justification for this procedure was provided by Stratford (2), it is now clear that the application of only the von-Karman momentum integral equation is not sufficiently accurate, since the important effects of incremental end wall work and losses are missing in the crude model. Moreover, the effects of tip leakage as well as secondary flow were not included in this model.

In incompressible flow through repeating stages, the wall boundary layer should grow to some asymptotic size and remain constant thereafter. On the other hand, the von-Karman equation, in the repeating stage situation, can only predict indefinitely growing layers until the inner and outer annulus layers merge.

Recognizing the insufficiency of von-Karman momentum integral equation to compressor annulus wall boundary layers, Mellor and Wood (3) proposed a new theory for integral representation of the end wall boundary layer. Inherent in the derivation is a description of the role of secondary flow,

tip clearance flows, blade force and the wall shear stress, thus providing a frame work for the incorporation of each of these effects into the overall problem. This theory needs empirical information such as shape factor, skin friction coefficient and leakage coefficient. This model is incorporated in performance calculations of axial compressor by Mellor and Balsa (4,5). Their predictions of compressor performance are good, except for the empirical parameters and absence of adjustable parameters. Hirsch (6) has applied Mellor and Wood (3) theory to predict overall performance of a single stage compressor. He has shown that the constant shape factor and skin friction coefficient assumptions are invalid. He has compared this theory with the existing data and has shown that skin friction coefficient takes up unusually high values at the tip of rotor blade. Finally, he reformulates the theory in streamline coordinates thus allowing for shape factor variation and the Reynolds number effects, introduces the wall skewing angle, modifies the original closure equation by allowing non-collateral character of the boundary layer at the blade outlet.

Railly (7) improved the theory of Mellor and Wood (3) by deriving a second equation for the growth of the end wall boundary layer which relates the work of the mean blade force along the mean velocity with the energy of secondary disturbances in the boundary layer. Secondary flow theory is used to obtain two equations for two boundary layer parameters. Railly and Sharma (8) compared Railly's (7) theory with experimental results downstream of a single stage rotor and have obtained good agreement between theory and experiment.

Work on annulus wall boundary layers in axial turbomachines, especially by the Cambridge University group was reviewed in Reference 9. Recently, Reynolds (10) conducted experiments on axial flow research fan of Applied

Research Laboratory of the Pennsylvania State University. He measured rotor exit flow up to one chord length downstream in the tip region, using a wedge probe and determined that the predominant flows in the end wall region of a compressor rotor were annulus wall boundary layer and tip leakage flows.

The blade boundary layer on a rotating blade and their interaction with the annulus wall boundary layer has been studied by the Pennsylvania State University group (11,12). Their experimental work is confined to axial flow inducer. The three-dimensional form of momentum integral equations is derived. Eventhough this work represents one extreme case, where viscous effects are large, the results are applicable to axial compressors and other turbomachinery.

II. ANALYSIS OF ROTOR BLADE END WALL FLOWS IN COMPRESSORS

2.1 Introduction

The objective of the analytical investigation is to model end wall flows including leakage and secondary flows, casing and blade boundary layers and to include it in the analysis and design of axial flow compressors. So far casing and blade boundary layers were included in the end wall flow model.

The approach for the analysis, the assumptions made and the important equations derived will be presented in the following sections.

The analysis is a preliminary one and is being continuously updated.

2.2 Nomenclature

C_1, C_2, C_3	Constants in Cole's velocity profile
C_4	$C_3 - 1$
C_5	$C_3 - 1/2$
C_6	$C_2\ (1 - 4/\pi^2)$
C_7	$\frac{C_3}{3} - \frac{1}{9}$
C_8	$C_2\ (\frac{1}{3} - \frac{2}{\pi^2})$
C_9	$C_4 + C_7$
C_{10}	$C_2 - C_6 + C_8$
C_{11}	$(C_3 - 2)\ C_3$
C_{12}	$2C_3 - 3C_2 + \frac{2C_2}{\pi}\ Si(\pi)$
C_{13}	$C_3\ C_4 + 1/2$
C_{14}	$C_2^2\ (\frac{3}{2} - 8/\pi^2)$
C_{15}	$C_{12} - \frac{8}{\pi} - \frac{6C_2}{\pi}\ Si(\pi)$

C_{16}	$(2 + 4/\pi)\ C_2$
C_{17}	$2\ (C_4 - C_5 - \frac{4}{9}\ C_3)$
C_{18}	$(2C_2^2 - C_{14} + \frac{4C_2^2}{\pi^2})$
C_{19}	$2C_2\ (\frac{4}{3} + \frac{2}{\pi^2}) + C_{16}$
C_{20}	$C_{12} + C_{15} + 2C_3\ (\frac{1}{3} - \frac{2}{\pi^2}) + C_2\ (\frac{7}{9} + \frac{2Si(\pi)}{\pi})$
C_{21}	$C_{11} + C_{13} + .2 + C_3\ (\frac{C_3}{3} - \frac{2}{9})$
C_{22}	$1/5$
C_{23}	$2C_4 - 4C_5 + 4\ (C_3 - \frac{1}{3}) + \frac{1}{2} - \frac{2}{25} + C_3\ (\frac{2}{5} + \frac{1}{2})$
C_{24}	$\frac{3}{2}\ C_2^2 - 2C_{14} + 6C_2\ (\frac{1}{2} + \frac{4}{\pi^2}) + (\frac{1}{5} - \frac{3}{2})\ C_2^2 + 8C_2$
C_{25}	$C_{12} - 2C_{15} - 2C_3\ (\frac{21}{25} + \frac{8}{\pi^2} + \frac{24}{\pi^4}) + C_2\ (\frac{74}{\pi}\ Si(\pi) + \frac{11}{2})$
C_{26}	$2C_3 - 2C_{16} + 48C_2\ (\frac{1}{\pi^2} - \frac{2}{\pi^4})$
q	Any flow quantity
r	Radial direction
x	Direction along the external streamline
y	Direction normal the the external streamline
u	Resultant flow velocity (time averaged)
U_τ	Skin friction velocity
$Si(\pi)$	$\int_0^t \frac{\sin t}{t}\ dt$
β	Air angle measured from axial direction
δ	Blade boundary layer thickness
δ_w	Annulus wall boundary layer thickness
ε_ω	Limiting streamline angle of the blade boundary layer
Π	Coles wake parameter
Ω	Angular velocity

θ	Tangential direction
θ_a	Angular pitch of the annulus wall boundary layer region between the blade boundary layers
$\overline{U}$	$\ell n \left(\frac{U_\tau \delta}{\nu}\right)$

Subscripts

p	Pressure surface of the blade
s	Suction surface of the blade
b	Blade surface
r,θ,z	Radial, tangential and axial directions respectively
s,n	Streamwise and normal directions respectively
1	Edge of blade boundary layer on suction surface
2	Edge of blade boundary layer on pressure surface

Superscripts

*	Refer to the boundary layer on the pressure side of the blade
-	Pitch average of fluctuating quantities
'	Spatial fluctuations
"	Temporal fluctuations

2.3 Assumptions

The following assumptions are made in the analysis of end wall flow

1. Flow is incompressible and steady relative to the rotor.
2. Blade camber is small.
3. Coles velocity profile is assumed for the blade boundary layer velocity in the z direction and Mager's velocity profile is assumed for the blade boundary layer velocity in the r direction.
4. β in the blade boundary layer is assumed to be constant in the tangential direction.

2.4 Approach

The time-averaged equations of continuity and momentum are written in rotating cylindrical coordinate system (see Fig. 2). Afterwards, the momentum equations are integrated in θ-direction. The integration is carried in three regions: 1) blade boundary layer on pressure side, 2) annulus wall boundary layer region between the two blade boundary layers and 3) blade boundary layer on suction side. In integrating momentum equations in blade boundary layers, Cole's profile for axial velocity and Mager's profile for radial velocity are used. Then the momentum equations are integrated in radial direction within the annulus wall boundary layer.

2.5 Momentum Integral Formulation

The continuity and momentum equations in cylindrical rotating coordinate system are given by,

continuity equation:

$$\frac{\partial u_z}{\partial z} + \frac{1}{r}\frac{\partial u_\theta}{\partial \theta} + \frac{\partial u_r}{\partial r} + \frac{u_r}{r} = 0 \qquad (1)$$

z - momentum equation:

$$u_z \frac{\partial u_z}{\partial z} + u_\theta \frac{\partial u_z}{r\partial \theta} + u_r \frac{\partial u_z}{\partial r} =$$

$$\frac{1}{\rho}\left[-\frac{\partial p}{\partial z} + \frac{\partial \tau_{zz}}{\partial z} + \frac{\partial \tau_{\theta z}}{r\partial \theta} + \frac{\partial \tau_{rz}}{\partial r} + \frac{\tau_{rz}}{r}\right] \qquad (2)$$

r - momentum equation:

$$u_z \frac{\partial u_r}{\partial z} + u_\theta \frac{\partial u_r}{r\partial \theta} + u_r \frac{\partial u_r}{\partial r} - \frac{1}{r}(u_\theta + \Omega r)^2 =$$

$$\frac{1}{\rho}\left[-\frac{\partial p}{\partial r}+\frac{\partial \tau_{zr}}{\partial z}+\frac{\partial \tau_{\theta r}}{r\partial\theta}+\frac{\partial \tau_{rr}}{\partial r}+\frac{\tau_{rr}}{r}\right] \tag{3}$$

θ - momentum equation:

$$u_z\frac{\partial u_\theta}{\partial z}+u_\theta\frac{\partial u_\theta}{r\partial\theta}+u_r\frac{\partial u_\theta}{\partial r}+\frac{u_r}{r}(u_\theta+2\Omega r)$$

$$=\frac{1}{\rho}\left[-\frac{1}{r}\frac{\partial p}{\partial\theta}+\frac{\partial \tau_{z\theta}}{\partial z}+\frac{\partial \tau_{\theta\theta}}{r\partial\theta}+\frac{\partial \tau_{r\theta}}{\partial r}+\frac{\tau_{r\theta}}{r}\right] \tag{4}$$

where,

$$\tau_{r\theta}=\mu\left(\frac{\partial u_\theta}{\partial r}+\frac{\partial u_r}{r\partial\theta}-\frac{u_\theta}{r}\right)-\rho\,\overline{u_r''u_\theta''}$$

$$\tau_{\theta z}=\mu\left(\frac{\partial u_z}{r\partial\theta}+\frac{\partial u_\theta}{\partial z}\right)-\rho\,\overline{u_\theta''u_z''}$$

$$\tau_{zr}=\mu\left(\frac{\partial u_r}{\partial z}+\frac{\partial u_z}{\partial r}\right)-\rho\,\overline{u_r''u_z''} \tag{5}$$

$$\tau_{\theta\theta}=2\mu\left(\frac{\partial u_\theta}{r\partial\theta}+\frac{u_r}{r}\right)-\rho\,\overline{u_\theta''^2}$$

$$\tau_{rr}=2\mu\frac{\partial u_r}{\partial r}-\rho\,\overline{u_r''^2}$$

$$\tau_{zz}=2\mu\frac{\partial u_z}{\partial z}-\rho\,\overline{u_z''^2}$$

Assumed velocity profiles in the blade boundary layer:

Cole's velocity profile is used for the blade boundary layer velocity in the z-direction.

Refer to the Fig. 2, let

$$\theta'=\theta-\theta_p \quad \text{or} \quad \theta-\theta_s$$

Then $$\frac{u_s}{U_\tau} = C_1 \left[\ell n \frac{U_\tau r\theta'}{\nu} + C_2 \Pi W \left(\frac{r\theta'}{\delta}\right) + C_3\right] \qquad (6)$$

where $U_\tau = \left(\frac{\tau_w}{\rho}\right)^{1/2}$, u_s is the streamwise velocity

τ_w = wall shear stress, ρ = density

$W = [1 - \cos\left(\frac{r\theta'}{\delta}\right)]$

C_1, C_2, C_3 are constants.

Π = Cole's wake parameter = f (z,r)

Mager's profile is used for the blade boundary layer velocity in the r-direction.

$$\frac{u_r}{u_s} = f\left(\frac{r\theta'}{\delta}\right) = \varepsilon_\omega (1 - \eta)^2 \qquad \text{where } \eta = \frac{r\theta'}{\delta} \qquad (7)$$

Hence,

$$\frac{u_r}{U_\tau} = \frac{u_r}{u_s}\frac{u_s}{U_\tau} = C_1 \left[\ell n \left(\frac{U_\tau r\theta'}{\nu}\right) + C_2 \Pi W \left(\frac{r\theta'}{\delta}\right) + C_3\right] \varepsilon_\omega (1 - \eta)^2 \qquad (8)$$

For the present formulation, normal velocity in the blade boundary layer is assumed to be very small compared to the streamwise velocity in the blade boundary layer.

Hence $u_z \simeq u_s \cos\beta$ and $u_\theta \simeq u_s \sin\beta$.

Integration in θ-direction from blade-to-blade:

Let q be any flow quantity, then (Fig. 2),

$$\int_{\theta_s}^{\theta_p} \frac{\partial q}{\partial z}\, d\theta = \int_{\theta_s}^{\theta_s+\theta_1} \frac{\partial q}{\partial z}\, d\theta + \int_{\theta_s+\theta_1}^{\theta_p-\theta_2} \frac{\partial q}{\partial z}\, d\theta + \int_{\theta_p-\theta_2}^{\theta_p} \frac{\partial q}{\partial z}\, d\theta \qquad (9)$$

where θ_1, θ_2 are tangential thicknesses of blade boundary layer on suction and pressure surfaces respectively.

Using the following relation for differentiation under integral sign,

$$\int_a^b \frac{\partial q}{\partial z}\, d\theta = \frac{\partial}{\partial z} \int_a^b q d\theta - q_b \frac{db}{dz} + q_a \frac{da}{dz} \tag{10}$$

Hence equation (9) becomes,

$$\int_{\theta_s}^{\theta_p} \frac{\partial q}{\partial z}\, d\theta = \frac{\partial}{\partial z} \int_{\theta_s}^{\theta_s+\theta_1} q d\theta - q_1 \frac{d}{dz}(\theta_s + \theta_1) + q_s \frac{d\theta_s}{dz} + \theta_a \frac{\partial \bar{q}}{\partial z}$$

$$- q_2 \frac{d}{dz}(\theta_p - \theta_2) + q_1 \frac{d}{dz}(\theta_s + \theta_1) + \frac{\partial}{\partial z} \int_{\theta_p-\theta_2}^{\theta_p} q d\theta - q_p \frac{d\theta_p}{dz} + q_2 \frac{d}{dz}(\theta_p - \theta_2)$$

Hence

$$\int_{\theta_s}^{\theta_p} \frac{\partial q}{\partial z}\, d\theta = \frac{\partial}{\partial z} \int_{\theta_s}^{\theta_s+\theta_1} q d\theta + \theta_a \frac{\partial \bar{q}}{\partial z} + \frac{\partial}{\partial z} \int_{\theta_p-\theta_2}^{\theta_p} q d\theta - q_p \frac{d\theta_p}{dz} + q_s \frac{d\theta_s}{dz} \tag{11}$$

Similarly $$\int_{\theta_s}^{\theta_p} \frac{\partial q}{\partial r}\, d\theta = \frac{\partial}{\partial r} \int_{\theta_s}^{\theta_s+\theta_1} q d\theta + \theta_a \frac{\partial \bar{q}}{\partial r} + \frac{\partial}{\partial r} \int_{\theta_p-\theta_2}^{\theta_p} q d\theta$$

$$- q_p \frac{d\theta_p}{dr} + q_s \frac{d\theta_s}{dr} \tag{12}$$

and $$\int_{\theta_s}^{\theta_p} \frac{\partial q}{\partial \theta}\, d\theta = q_p - q_s \tag{13}$$

Now integrating the equations of motion in the θ-direction, and using the continuity equation in the momentum equations, we obtain the following equations.

Continuity equation:

$$\frac{\partial \bar{u}_z}{\partial z} + \frac{\partial \bar{u}_r}{\partial r} + \frac{\bar{u}_r}{r} + X = o \tag{14}$$

z-momentum equation:

$$\bar{u}_z \frac{\partial \bar{u}_z}{\partial z} + \bar{u}_r \frac{\partial \bar{u}_z}{\partial r} + \frac{C_1}{\theta_a r}\left[\frac{\partial}{\partial z}(C + C^*) + \frac{\partial}{\partial r}(D + D^*)\right]$$

$$- \bar{u}_z X = \frac{1}{\rho}\left\{\left[-\frac{\partial \bar{p}}{\partial z} + \frac{\Delta p}{\theta_a r}\tan\bar{\beta} + \frac{\partial \bar{\tau}_{zz}}{\partial z}\right.\right.$$

$$\left. + \frac{1}{r}\frac{\partial}{\partial r}(r\,\bar{\tau}_{rz})\right] + \frac{1}{\theta_a}\left[\frac{2\bar{\tau}_{bz}}{r} - \frac{\partial}{\partial z}(I_1 + I_1^*)\right.$$

$$\left. + \frac{\partial}{\partial z}(I_2 + I_2^*) + \frac{1}{r}\frac{\partial}{\partial r}(l_3 + I_3^*) - \bar{\tau}_{zz_p}\frac{\partial \theta_p}{\partial z}\right.$$

$$+ \bar{\tau}_{zz_s} \frac{\partial \theta_s}{\partial z} - \tau_{rz_p} \frac{\partial \theta_p}{\partial r} + \bar{\tau}_{rz_s} \frac{\partial \theta_s}{\partial r}] \, d\theta\} \qquad (15)$$

r-momentum equation:

$$\bar{u}_z \frac{\partial \bar{u}_r}{\partial z} + \bar{u}_r \frac{\partial \bar{u}_r}{\partial r} + \frac{\overline{u_z^2 \tan^2\beta}}{r} + 2\Omega \, \overline{u_z \tan\beta}$$

$$+ \Omega^2 (r + \delta + \delta^*) - \bar{u}_r X + \frac{c_1^2}{\theta_a r} [\frac{\partial}{\partial z} (D + D^*) + \frac{\partial}{\partial r} (E + E^*)$$

$$+ (C\tan^2\beta + C^* \tan^2\beta^*) + \frac{2\Omega r}{C_1} (A\tan\beta + A^* \tan\beta^*)]$$

$$= \frac{1}{\rho} \{[- \frac{\partial \bar{p}}{\partial r} + \frac{\partial \bar{\tau}_{zr}}{\partial z} + \frac{1}{r} \frac{\partial}{\partial r} (r\bar{\tau}_{rr}) + \frac{2}{r} \frac{\bar{\tau}_{br}}{\theta_a}]$$

$$+ \frac{1}{\theta_a} [- \frac{\partial}{\partial r} (I_1 + I_1^*) + \frac{1}{r} \frac{\partial}{\partial z} (I_3 + I_3^*) + \frac{1}{r} \frac{\partial}{\partial r} (I_5 + I_5^*)$$

$$+ p_p \frac{\partial \theta_p}{\partial r} - p_s \frac{\partial \theta_s}{\partial r} - \tau_{zr_p} \frac{\partial \theta_p}{\partial z} + \tau_{zr_s} \frac{\partial \theta_s}{\partial z} - \tau_{rr_p} \frac{\partial \theta_p}{\partial r}$$

$$+ \bar{\tau}_{rr_s} \frac{\partial \theta_s}{\partial r}] \, d\theta\} \tag{16}$$

θ-momentum equation:

$$\bar{u}_z \frac{\partial}{\partial z} (\overline{u_z \tan\beta}) + \bar{u}_r \frac{\partial}{\partial r} (\overline{u_z \tan\beta}) + \frac{\overline{u_z u_r \tan\beta}}{r} + 2\bar{u}_r \Omega - \overline{u_z \tan\beta}$$

$$+ \frac{C_1^2}{\theta_{ar}} [\frac{\partial}{\partial z} (C\tan\beta + C^* \tan\beta^*) + \frac{1}{r} \frac{\partial}{\partial r} (Dr\tan\beta + D^* r \tan\beta^*) + \frac{2\Omega}{C_1} (B + B^*)]$$

$$= \frac{1}{\rho} \{[- \frac{\Delta p}{r\theta_a} + \frac{\partial \bar{\tau}_{z\theta}}{\partial z} + \frac{2\bar{\tau}_{b\theta}}{r} + \frac{1}{r} \frac{\partial}{\partial r} (r\bar{\tau}_{r\theta})] + \frac{1}{\theta_a} [\frac{\partial}{\partial z} (I_4 + I_4^*)$$

$$+ \frac{1}{r} \frac{\partial}{\partial r} (I_6 + I_6^*) - \tau_{z\theta_p} \frac{\partial \theta_p}{\partial z} + \tau_{z\theta_s} \frac{\partial \theta_s}{\partial z} - \tau_{r\theta_p} \frac{\partial \theta_p}{\partial r} + \tau_{r\theta_s} \frac{\partial \theta_s}{\partial r}] \tag{17}$$

where

$$A = U_\tau \cos\beta \, \delta \, (\bar{U} + C_2 \Pi + C_4)$$

$$A^* = U_\tau^* \cos\beta' \, \delta^* \, (\bar{U}^* + C_2 \Pi^* + C_4)$$

$$B = U_\tau \delta \, \varepsilon_\omega \, (\frac{\bar{U}}{3} + C_9 + C_{10} \Pi)$$

$$B^* = U_\tau^* \delta^* \, \varepsilon_\omega^* \, (\frac{\bar{U}^*}{3} + C_9 + C_{10} \Pi^*)$$

Then

$$X = \frac{C_1}{\theta_a r}\left[\frac{\partial}{\partial z}(A + A^*) + \frac{\partial}{\partial r}(B + B^*)\right]$$

$$C = U_\tau^2 \cos^2\beta\,\delta\,[\bar{u}^2 + 2C_4\bar{u} + \tfrac{3}{2}C_2^2\Pi^2 + 2C_2\Pi\bar{u} + C_{11} + C_{12}\Pi]$$

$$C^* = U_\tau^{*2} \cos^2\beta^*\,\delta^*\,[\bar{u}^{*2} + 2C_4\bar{u}^{*2} + \tfrac{3}{2}C_2^2\Pi^{*2} + 2C_2\Pi^*\bar{u}^* + C_{11} + C_{12}\Pi]$$

$$D = U_\tau^2\,\varepsilon_\omega \cos\beta\,\delta\,[\tfrac{\bar{u}^2}{3} + C_{17}\bar{u} + C_{18}\Pi^2 + C_{19}\Pi\bar{u} + C_{20}\Pi + C_{21}]$$

$$D^* = U_\tau^{*2}\,\varepsilon_\omega^* \cos\beta^*\,\delta^*\,[\tfrac{\bar{u}^{*2}}{3} + C_{17}\bar{u}^* + C_{18}\Pi^{*2} + C_{19}\Pi^*\bar{u}^* + C_{20}\Pi^* + C_{21}]$$

$$E = U_\tau^2\,\varepsilon_\omega^2\,\delta\,[C_{22}\bar{u}^2 + C_{23}\bar{u} + C_{24}\Pi^2 + C_{25}\Pi + C_{26}\Pi\bar{u} + C_{27}]$$

$$E^* = U_\tau^{*2}\,\varepsilon_\omega^{*2}\,\delta^*\,[C_{22}\bar{u}^{*2} + C_{23}\bar{u}^* + C_{24}\Pi^{*2} + C_{25}\Pi^* + C_{26}\Pi^*\bar{u}^* + C_{27}]$$

$$I_1 = \int_{\theta_s}^{\theta_s+\theta_1} p\,d\theta \qquad I_1^* = \int_{\theta_p-\theta_2}^{\theta_p} p\,d\theta$$

$$I_2 = \int_{\theta_s}^{\theta_s+\theta_1} \tau_{rz}\,d\theta \qquad I_2^* = \int_{\theta_p-\theta_2}^{\theta_p} \tau_{rz}\,d\theta$$

$$I_3 = r\int_{\theta_s}^{\theta_s-\theta_1} \tau_{rz}\,d\theta \qquad I_3^* = r\int_{\theta_p-\theta_2}^{\theta_p} \tau_{rz}\,d\theta$$

$$I_4 = \int_{\theta_s}^{\theta_s+\theta_1} \tau_{z\theta}\,d\theta \qquad I_4^* = \int_{\theta_p-\theta_2}^{\theta_p} \tau_{z\theta}\,d\theta$$

$$I_5 = r \int_{\theta_s}^{\theta_s+\theta_1} \tau_{rr} d\theta \qquad I_5^* = r \int_{\theta_p-\theta_2}^{\theta_p} \tau_{rr} d\theta$$

$$I_6 = r \int_{\theta_s}^{\theta_s+\theta_1} \tau_{r\theta} d\theta \qquad I_6^* = r \int_{\theta_p-\theta_2}^{\theta_p} \tau_{r\theta} d\theta \qquad (18)$$

In equation (15) to (18) the starred quantities refer to boundary layer on pressure side of the blade.

Let δ_w = annulus wall boundary layer thickness.

$\bar{U}_e$ = pitch averaged velocity at the edge of the annulus wall boundary layer.

$= \bar{U}_e(z)$

The assumption that $\bar{U}_e$ is a function of z only is valid in the end wall region. In the other regions $\bar{U}_e$ is a function of both z and r.

Define the following annulus wall boundary layer thicknesses.

$$\delta_1 = \int_{r_t-\delta_w}^{r_t} (1 - \frac{\bar{u}_z}{\bar{U}_e})\, dr$$

$$\delta_2 = \int_{r_t-\delta_w}^{r_t} \frac{\bar{u}_r}{\bar{U}_e}\, dr$$

$$\theta_{11} = \int_{r_t-\delta_w}^{r_t} (1 - \frac{\bar{u}_z}{\bar{U}_e}) \frac{\bar{u}_z}{\bar{U}_e}\, dr$$

$$\theta_{22} = \int_{r_t-\delta_w}^{r_t} (\frac{\bar{u}_r}{\bar{U}_e})^2\, dr$$

$$\theta_{12} = \int_{r_t-\delta_w}^{r_t} \left(1 - \frac{\bar{u}_r}{\bar{U}_e}\right)^2 dr$$

and

$$\theta_{21} = \int_{r_t-\delta_w}^{r_t} \frac{\bar{u}_z \bar{u}_r}{\bar{U}_e^2} dr \qquad (19)$$

Multiplying continuity equation by $(\bar{u}_z - \bar{U}_e)$ and adding to the z-momentum equation and then integrating the resulting equation with respect to r from $(r_t - \delta_w)$ to r_t, we get the z-momentum integral equation

$$\frac{\partial \theta_{11}}{\partial z} + (2 + H) \frac{\theta_{11}}{\bar{U}_e} \frac{\partial \bar{U}_e}{\partial z} - \frac{1}{\bar{U}_e} \int_{r_t-\delta_w}^{r_t} \left(\frac{\partial \bar{U}_e}{\partial z} + X\right) dr - \frac{(\theta_{21} - \delta_2)}{r_m}$$

$$= \frac{1}{\rho \bar{U}_e^2} \int_{r_t-\delta_w}^{r_t} \text{R.H.S. of Eq. (24)} \qquad (20)$$

where

$$H = \text{shape factor} = \frac{\delta_1}{\theta_{11}}$$

and

$$r_m = r_t - \frac{\delta_w}{2}$$

Similarly we get the r-momentum equation.

$$\frac{\partial \theta_{22}}{\partial r} + \frac{\partial}{\partial r} (\theta_{21} + \delta_1) + \frac{1}{\bar{U}_e} \left[(2\theta_{21} + \delta_1) \frac{\partial \bar{U}_e}{\partial z} - \int_{r_t-\delta_w}^{r_t} \frac{\partial \bar{U}_e}{\partial z} dr\right]$$

$$+ \frac{1}{r_m} (\theta_{22} - \delta_2) - \frac{1}{\bar{U}_e^2} \int_{r_t-\delta_w}^{r_t} \left[\bar{U}_e X + \frac{\overline{u_z^2 \tan^2\beta}}{r_m} + \overline{2\Omega u_z \tan\beta}\right.$$

$$+ \Omega^2 (r + \delta + \delta^*)] \, dr = \frac{1}{\rho U_e^2} \int_{r_t - \delta_w}^{r_t} \text{R.H.S. of Eq. (25)} \qquad (21)$$

where δ^* is the thickness of the boundary layer on the pressure side of the blade.

III. EXPERIMENTAL FACILITY, INSTRUMENTATION AND TECHNIQUE

Modifications to the compressor unit: An overall view of the compressor unit is shown in Fig. 3. A rotating traverse mechanism was mounted on the rotor shaft immediately after the rotor. This mechanism rotates at the same speed as the rotor. This mechanism along with the rotor was dynamically balanced at the Applied Research Laboratory of The Pennsylvania State University.

The traverse mechanism is capable of giving three degrees of freedom to the probe used in the end wall measurements. One mode is automatic and the two other modes are manual. Tangential movement of the probe is automatic and is achieved by mounting the probe on a disc which is rotated at an angular interval of 1/10 degree by a step motor. Radial and axial movements of the probe are to be carried out manually. The traverse mechanism has six axial slots on its periphery. The circumferential length of these slots allows measurements in two adjacent blade passages of the rotor in the end wall region of the blade. The axial spacings of the slots give accessibility for measuring the flow in the end wall region at various axial stations right from the leading edge of the rotor blade to its trailing edge. Provision has been made for measuring the hub wall and the blade static pressures.

The transverse mechanism is mounted immediately after the rotor. A scanivalve will be used to transmit blade static pressures and hub wall static pressures.

Instrumentation: The instrumentation assembly designed for transmitting the electrical and mechanical signals from a rotating reference frame to stationary instruments is shown in Fig. 4. This instrumentation

assembly enables transmission of data from a five-hole pitot probe and a three sensor hotwire. The assembly consists of a pressure transfer device (PTD 1) with a scanivalve mounted in it, a six-channel brush slip ring, a three-channel pressure transfer device (PTD), a six-channel mercury slip ring and a slotted disk. The PTD 1 and PTD will be used to transmit rotor blade static pressures, hub wall pressures immediately after the rotor and pressure measurements from the five-hole probe. The mercury slip ring will be used to transmit signals from the hotwire. The brush slip ring unit will be used to drive the step motors in the scanivalve and the rotating traverse mechanism. A photo cell mounted on the support plate of the instrumentation assembly will be used to measure the speed of the rotor accurately. The disk with slots will activate the photo cell.

At present the instrumentation is being assembled. The assembly will be connected to the rotor shaft by means of a flexible coupling to reduce transmission of rotor shaft eccentricity to the assembly. The instrumentation will be enclosed in a stationary housing to avoid flow distribution upstream of the rotor.

IV. STATUS OF EXPERIMENTAL WORK

The experimental work carried so far consists of determination of the overall characteristics of the compressor, velocity distributions at the inlet of IGV and after each blade row, check for axisymmetry, check for unsteadiness at the inlet. Wherever possible, these results are compared with those of Smith (13). In the following sections, a brief summary of the results and interpretation is given.

Overall characteristics: The compressor was tested extensively with various configurations both with the auxiliary fan and without auxiliary fan, to get the maximum pressure rise. It was decided to retain the auxiliary fan permanently in the facility. All tests were carried out with the auxiliary fan operating at constant speed and the compressor rotor operating at 1100 r.p.m. The throttle setting was varied to determine the performance characteristics of the compressor at various flow coefficients. The procedure for these tests was as follows.

For each throttle setting, total pressure, static pressure and flow angle traverses were taken using pitot probe and two-hole wedge probe, at four axial stations 1, 2, 3 and 5. The wall static pressures were also taken at the hub and the casing to check the validity of static pressure traverses. Radial distribution of axial and tangential velocities and stagnation pressure coefficient were determined from the measured data. By integrating over the annulus, the mass-averaged pressure-rise coefficient $\bar{\psi}^*$ was determined. The flow coefficient $\bar{\phi}$ was determined by integrating the axial velocity profile at the IGV inlet over the annulus area. Similarly $\bar{\phi}$ was determined at other axial stations and compared with $\bar{\phi}$ at the inlet of IGV. For the four runs that have been made, the flow

*These and other notations are defined at the end of this section.

coefficients after IGV, rotor and stator agree within 4% with the flow coefficient determined from velocity profile at IGV inlet.

A plot of the pressure-rise coefficient $\bar{\psi}$ vs. flow coefficient $\bar{\phi}$ is shown in Fig. 5. With the present arrangement, the throttle cannot be opened any further than that corresponding to the highest capacity data point in the figure. Smith's data was also plotted in the same figure. In general, the present curve is lower than that of Smith by about 10%.

Radial distribution of flow properties: In Fig. 6, the tangential and axial velocity distributions, flow angle and local pressure-rise coefficient distributions for $\bar{\phi} = 0.516$ (design) are shown. Also shown in the same figure are the design values as well as the measured values of Smith (13). Agreement between the radial distribution of axial velocity in both cases is good, the major discrepancy being observed at the hub and tip. The tangential velocity and flow angle distributions are about 10% lower than those measured by Smith and 5% lower than design values.

In the same figure, design distribution of axial and tangential velocities are shown. These distributions are obtained by axisymmetric design method which does not include secondary flow effects. Smith observed that the difference between his measured tangential velocity distribution and design distribution is due to the over-turning in the guide vanes.

In Fig. 7 radial distributions of relative flow quantities at rotor exit at $\bar{\phi} = 0.516$ for the present configuration, measured quantities by Smith (13) and design values are presented. In general, $\frac{W_\theta}{U_t}$, $\frac{W}{U_t}$ and β for the present case are higher than those obtained by Smith. This is to be expected, since $\frac{V_\theta}{Ut}$ is lower for the present case.

Design and measured velocity diagrams at six radial locations for the compressor stage is shown in Fig. 8. For inlet guide vanes, the agreement between design and measured velocity diagrams is good except at the hub and tip. This may be due to the secondary flow, which is not included in the design velocity diagram. The agreement between design and measured velocity triangles at rotor inlet is poor. The reason for this discrepancy is not evident. The agreement between design and measured velocity diagrams at rotor is good except at the tip. Here the difference is considerable. This may be due to tip leakage flows.

Stator inlet angles are those measured at the rotor exit. Hence the design and measured velocity diagrams are in good agreement. The spacing between rotor and stator is more than that of Smith (13). Hence the stator inlet flow is different from that of Smith. So the stator exit velocity diagrams are different from the design velocity diagrams.

Axisymmetry and unsteadiness test: Results of this test are shown in Fig. 9. Radial surveys of the mean velocity and turbulence intensities were measured by a single hot-wire at inlet to the IGV at three circumferential stations, shown in the insert of Fig. 9.

Turbulence intensities at stations 1 and 2 were in good agreement and usually less than 2%. Turbulence intensities at station 3 are higher than those at the other two stations. This may be due to the proximity of station 3 to the floor.

Nomenclature for Chapter IV

r	radius
r_h	hub radius
r_t	rotor tip radius
ΔP	total pressure rise across the rotor
U_t	rotor tip velocity
W	relative velocity
α	absolute flow angle
β	relative flow angle
$\bar{\phi}$	mass averaged flow coefficient

$$= \int_{r_h}^{r_t} V_x \, r dr \Big/ \int_{r_h}^{r_t} r dr$$

ψ_ℓ	local pressure rise coefficient $= \frac{2\Delta P}{\rho U_t^2}$
$\bar{\psi}$	mass averaged pressure rise coefficient

$$= \int_{r_h}^{r_t} \psi_\ell \, V_x r dr \Big/ \int_{r_h}^{r_t} V_x r dr$$

Subscripts

1	inlet to a blade row
2	exit of a blade row
x	axial direction
θ	tangential direction

REFERENCES

1. Jansen, W., "The Application of End Wall Boundary Layer Effects in the Performance Analysis of Axial Compressors," ASME Paper No. 67-WA/GT-11.

2. Stratford, B. S., "The Use of Boundary Layer Technique to Calculate the Blockage From the Annulus Boundary Layer in a Compressor," ASME Paper No. 67-WA/GT-1.

3. Mellor, G. L. and Wood, G. M., "An Axial Compressor End Wall Boundary Layer Theory," Journal of Basic Engineering, Transactions of the ASME Series D, June 1971, pp. 300-316.

4. Mellor, G. L. and Balsa, T. F., "The Prediction of Axial Compressor Performance with Emphasis on the Effect of Annulus Wall Boundary Layers," AGARDograph No. 164, 1972.

5. Balsa, T. F. and Mellor, G. L., "The Simulation of Axial Compressor Performance Using an Annulus Wall Boundary Layer Theory," Journal of Engineering for Power, Transactions of the ASME, Series B, July 1974.

6. Hirsch, Ch., "End Wall Boundary Layers in Axial Compressors," Journal of Engineering for Power, Transactions of the ASME Series B, Oct. 1974, pp. 413-426.

7. Railly, J. W., "A Non-Axisymmetric End Wall Boundary Layer Theory for Axial Compressor Rows," ARC CP 1322, 1975.

8. Railly J. W. and Sharma, P. B., "Treatment of the Annulus Wall Boundary Layer Using a Secondary Flow Analysis," ASME Paper No. 76-GT-52.

9. Horlock, J. H. and Perkins, H. J., "Annulus Wall Boundary Layers in Turbomachines," AGARDograph No. 185, 1974.

10. Reynolds, B., "Experimental Investigations of End Wall Flows in Aircraft Engine Compressors," B.S. Thesis, Department of Aerospace Engineering, The Pennsylvania State University, March 1976.

11. Lakshminarayana, B., et al., "Turbulent Boundary Layer on a Rotating Helical Blade," Journal of Fluid Mechanics, 1972, Vol. 51, Part 3, pp. 545-569.

12. Anand, A. K. and Lakshminarayana, B., "Three-Dimensional Turbulent Boundary Layer in a Rotating Helical Channel," Journal of Fluids Engineering, Transactions of the ASME, Series E., June 1975, pp. 197-210.

13. Smith, L. H., Jr., "Three-Dimensional Flow in Axial Flow Turbomachinery Part II. Experimental Investigations," Report I-14a, Institute for Co-operative Research, The Johns Hopkins University, 1953.

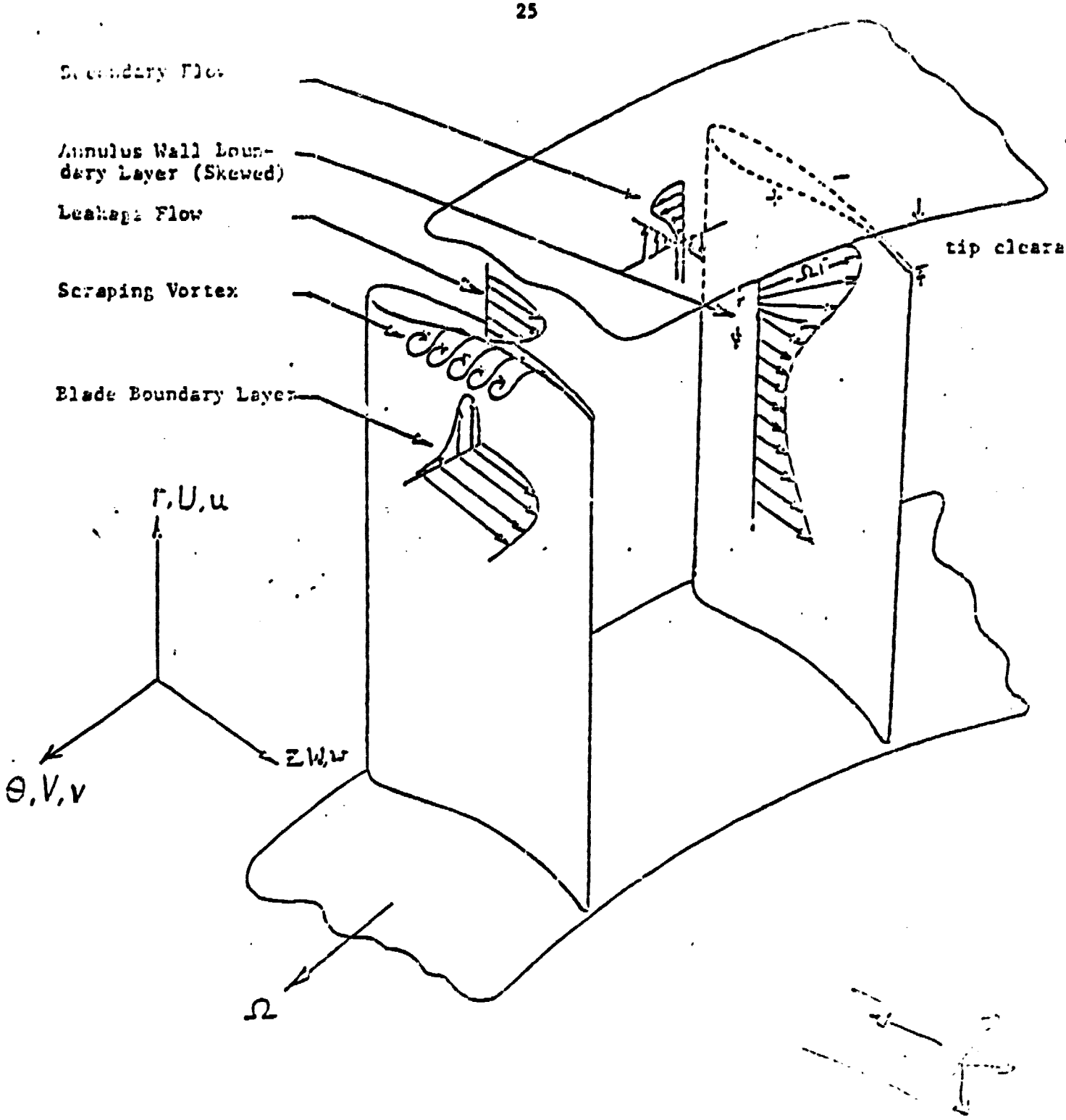

Figure 1: Qualitative Nature of End Wall Flows

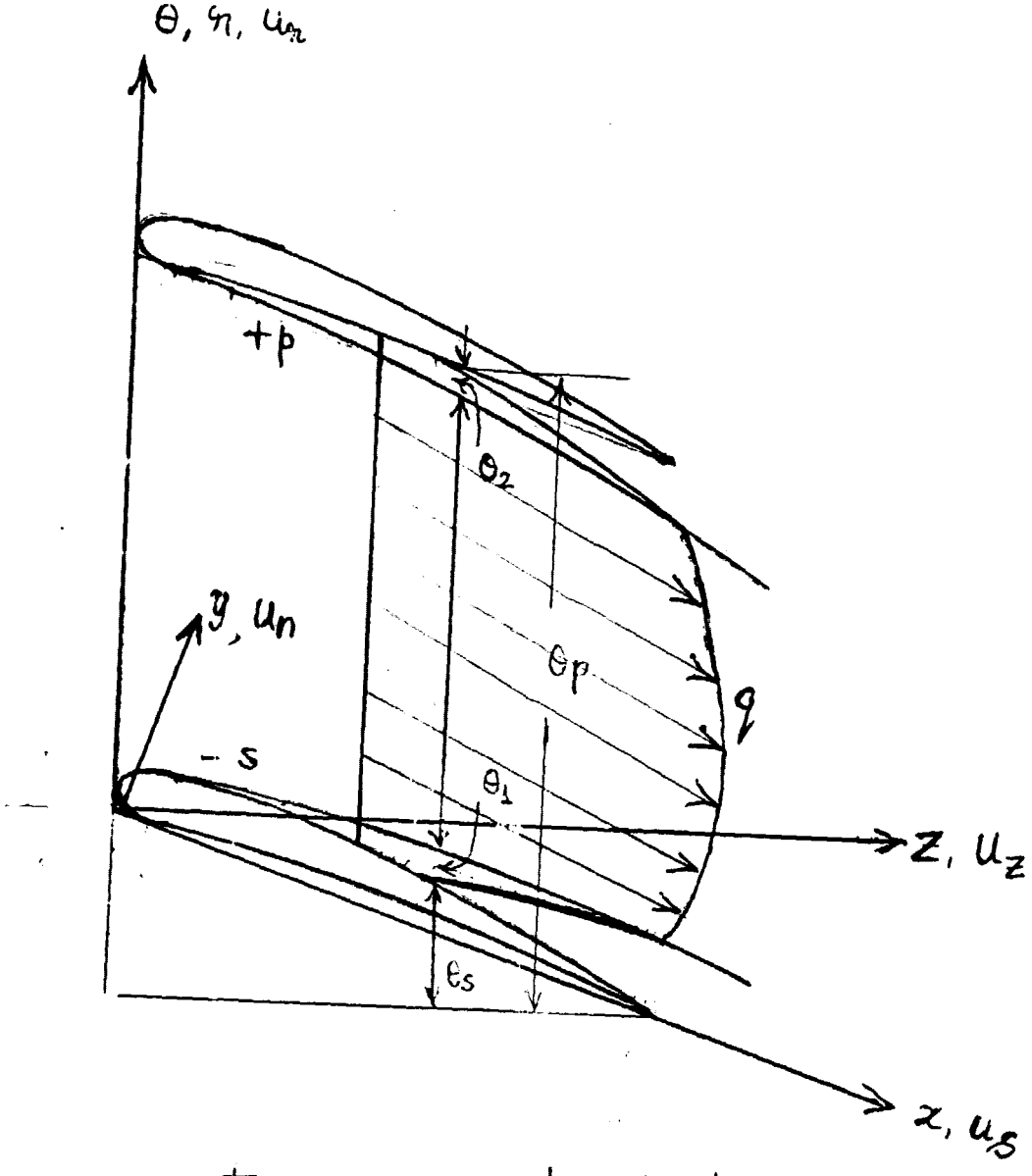

η- direction is normal to the plane of paper

Fig. 2 Co-ordinate System

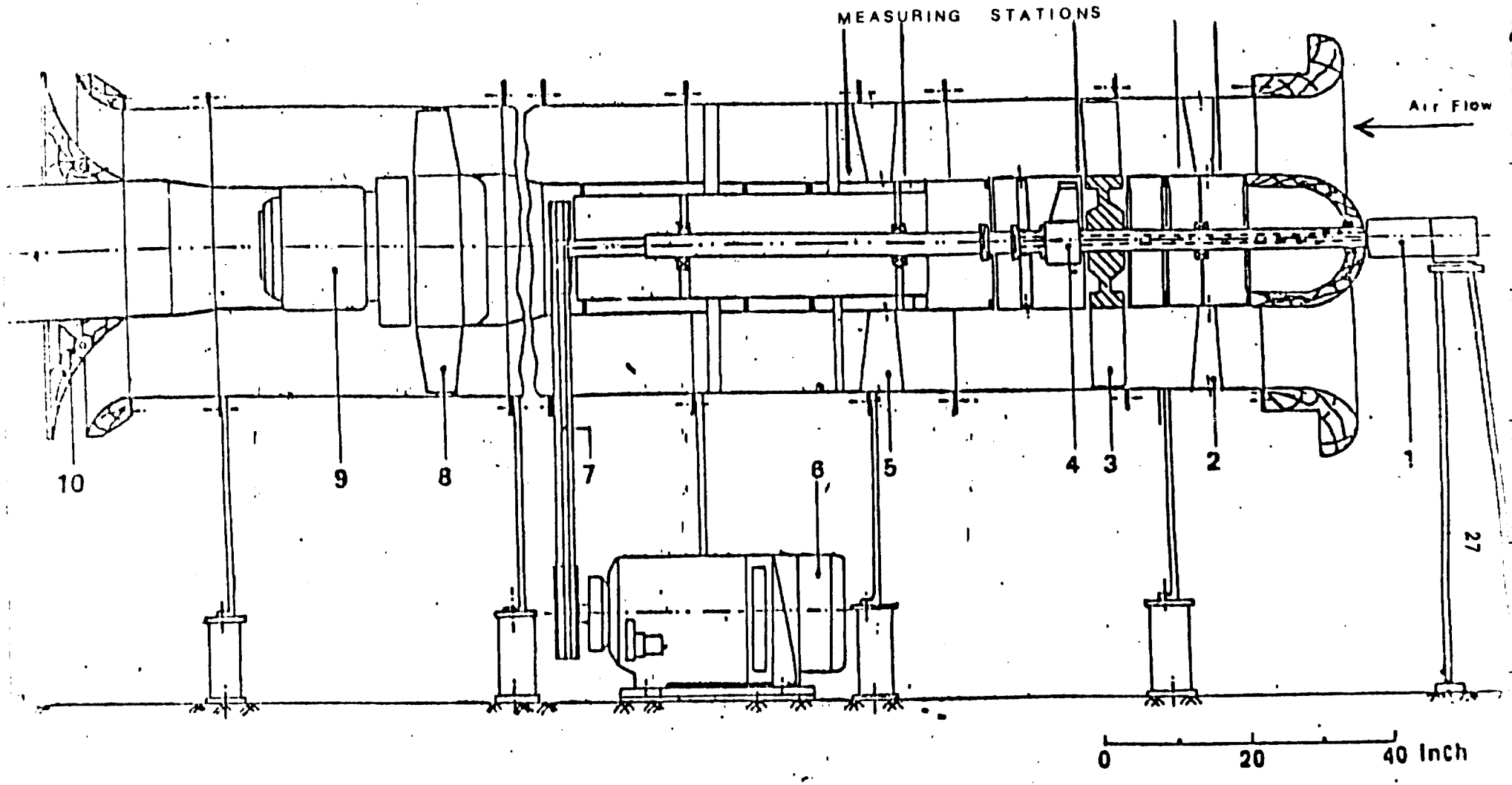

1. Signal Transfer System
2. I.G.V.
3. Compressor Rotor
4. Traverse Mechanism
5. O.G.V.
6. Compressor Drive Motor
7. Belt Drive
8. Aux. Fan Rotor
9. Fan Motor
10. Throttle

FIG 3. AXIAL FLOW COMPRESSOR TEST FACILITY

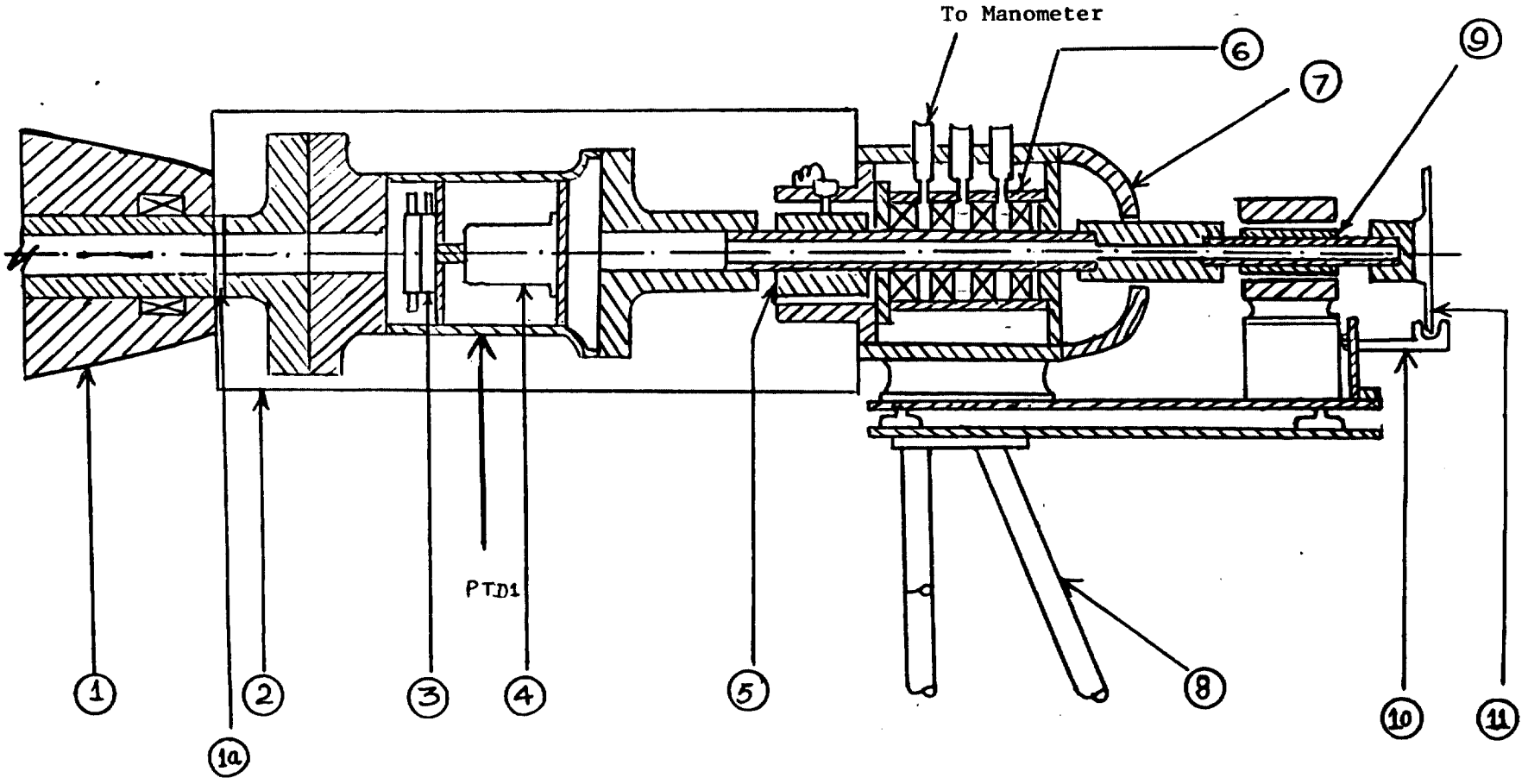

1. Compressor Nose
1a. Flexible Coupling
2. Housing
3. Scanivalve
4. Step Motor
5. Brush Slipring
6. Pressure Transfer Device
7. Cowling
8. Leveling Stand
9. Mercury Slipring
10. Photo Cell Support
11. Disk With 60 Slots

Fig 4. Instrumentation Assembly

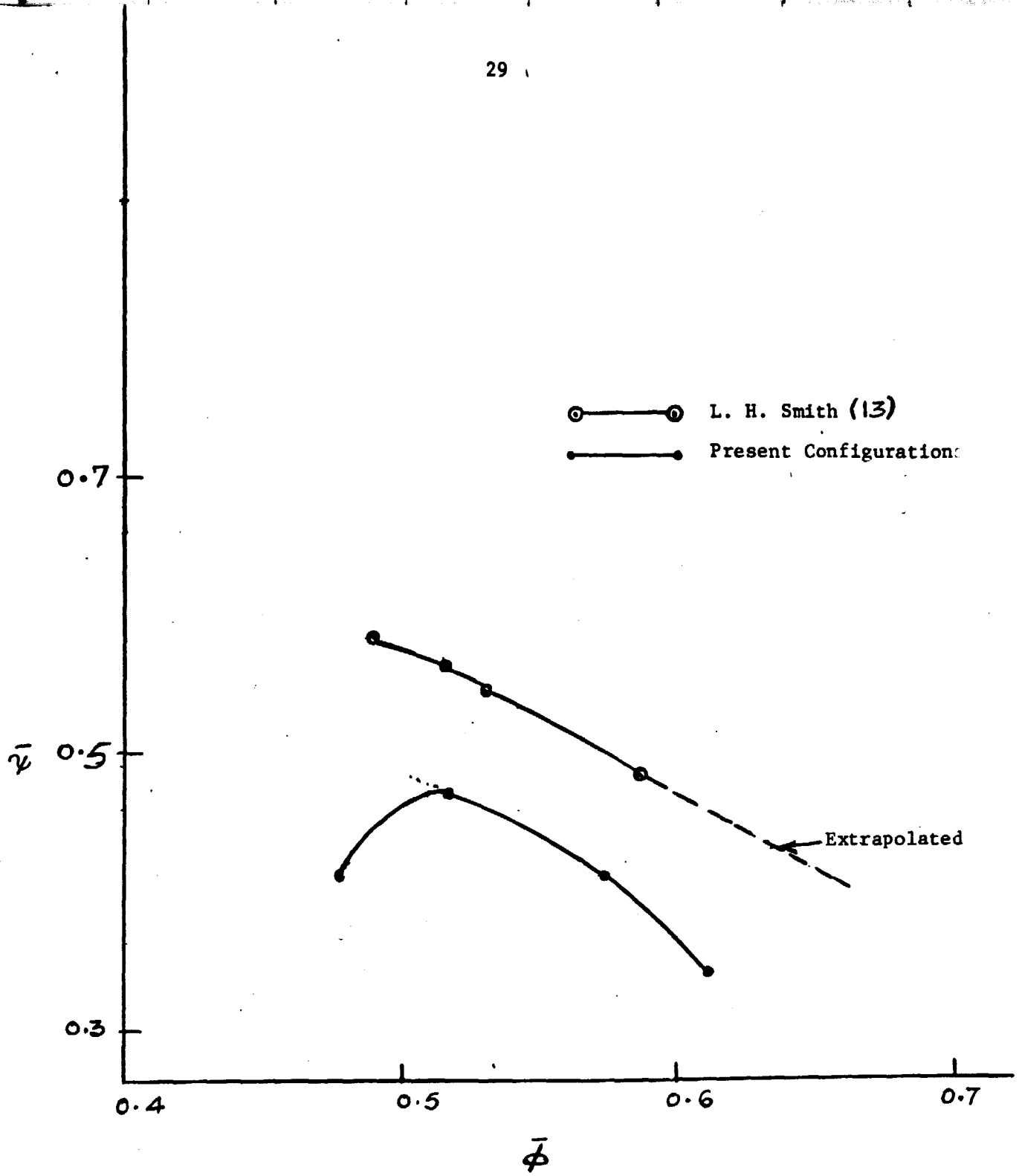

Fig. 5 Pressure Rise Coefficient vs. Flow Coefficient

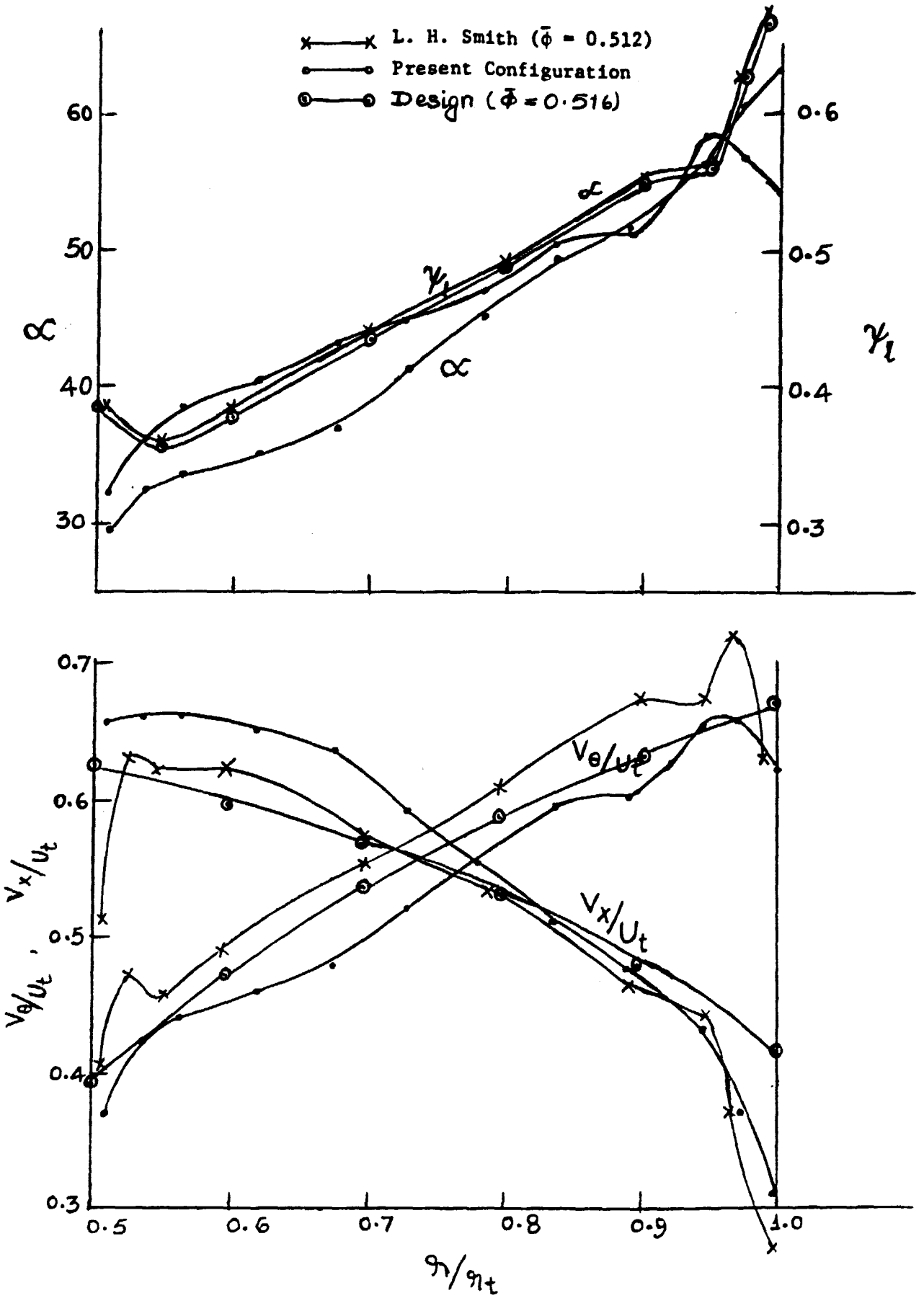

Fig. 6: Radial Distribution of Axial Velocity (V_x/U_t), Tangential Velocity (V_θ/U_t), Flow Angle (α) and Pressure Rise Coefficient (ψ_l) at Rotor Exit at $\bar{\phi}$ = 0.516, $\bar{\psi}$ = 0.466.

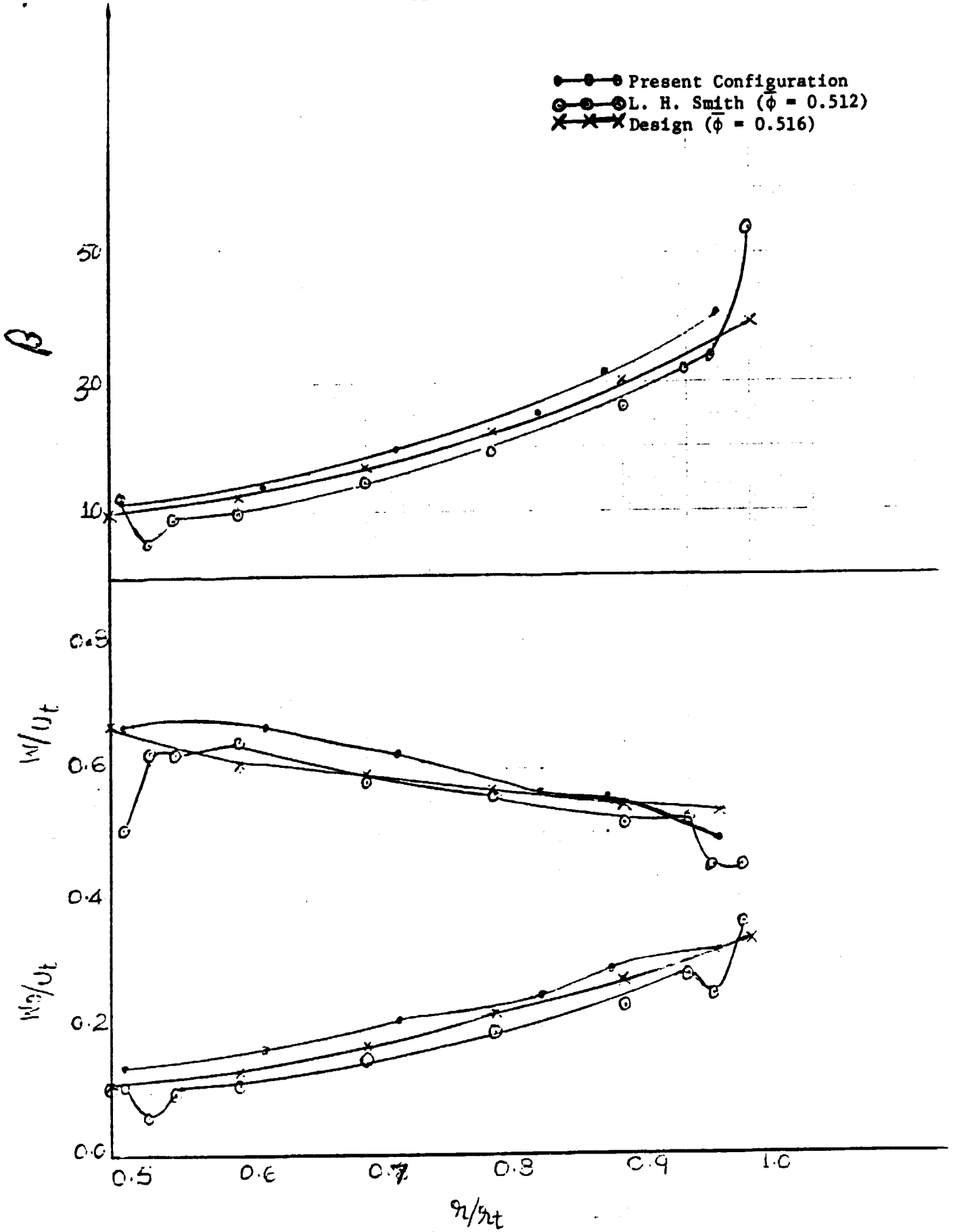

Fig. 7. Radial Distribution of W_θ/U_t, W/U_t and β at Rotor Exit at $\bar{\phi}$ = 0.516 and $\bar{x}$ = 0.466.

	r/r_{tip} = 1.0	0.9	0.8	0.7	0.6	0.5
IGV						
	Measured α_2 32.4	26.8	24.1	14.6	8.2	0
	Design α_2 44.2	25.5	17.0	12.0	-3	-7
ROTOR						
	Measured β_1 63.6	57.8	52.7	48.6	45.0	41.8
	Design β_1 57.2	51.9	55.6	52.8	52.3	51.8
	Measured β_2 42.0	32.1	24.1	18.0	13.4	10.6
	Design β_2 51.4	32.4	23.6	20.0	13.9	13.0
STATOR						
	Measured α_1 63.0	52.0	46.0	38.0	34.0	28.0
	Design α_1 61.2	55.8	51.1	16.6	12.8	38.2
	Measured α_2 13.0	34.0	26.0	16.0	12.5	0.6
	Design α_2 53.4	44.7	35.4	24.4	13.6	0.0

Fig 8. Measured (solid lines) and Design (Broken lines) Velocity Diagrams for Axial Flow Compressor Stage.

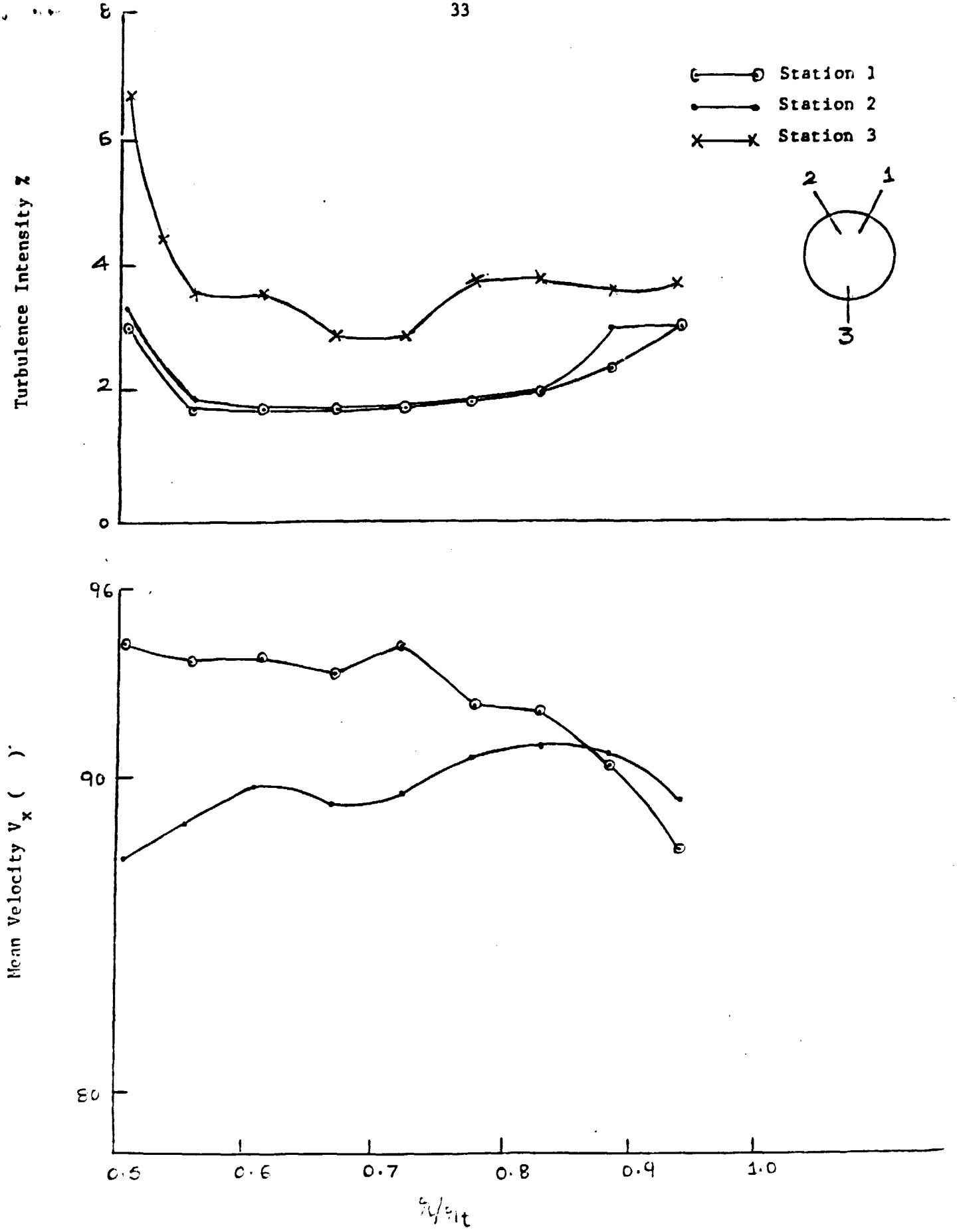

Fig. 9: Radial Distribution Inlet Velocities and Turbulence Intensities at Three Circumferential Stations